



Numerical and theoretical prediction of the thermodynamic response in marine LNG fuel tanks under sloshing conditions

Zhongdi Duan^{a,b}, Yifeng Zhu^{c,d}, Chenbiao Wang^{a,b}, Yuchao Yuan^{a,b,*}, Hongxiang Xue^{a,b}, Wenyong Tang^{a,b}

^a State Key Laboratory of Ocean Engineering, Shanghai Jiao Tong University, Shanghai, 200240, China

^b Collaborative Innovation Center for Advanced Ship and Deep-Sea Exploration, Shanghai, 200240, China

^c China Ship Research Center, Wuxi, 214082, China

^d Taihu Laboratory of Deepsea Technological Science, Wuxi, 214082, China

ARTICLE INFO

Keywords:

LNG fuel tank
Sloshing effect
Thermodynamic response
Depressurization
Thermal non-equilibrium

ABSTRACT

Liquefied natural gas (LNG) is becoming an attractive alternative fuel for the ship industry, while its storage in cryogenic LNG fuel tanks encounters complex thermodynamic responses under sea conditions and largely affects system operation reliability. This paper aims to investigate the sloshing effects on the thermodynamic responses of marine LNG fuel tanks by numerical modeling and theoretical analysis. A three-dimensional dynamic model is established to predict the coupled pressure–temperature evolution inside the tank under sloshing conditions. The liquid sloshing motions and the phase transition at the liquid–vapor interface are calculated by incorporating the sloshing and phase change sub-models. The effectiveness of the model to simulate liquid sloshing and tank thermodynamic response is verified by corresponding experimental data. The simulation results indicate that the model can reflect the major dynamics of pressure variation, temperature stratification and phase transition under sloshing excitation, and show that the sloshing uniforms LNG temperature, enhances interfacial mass-heat transfer, and accelerates tank depressurization. A theoretical expression that characterizes the relations between tank pressure drop, vapor temperature and condensation is derived, showing a good correlation with numerical results and providing a feasible way for the inverse determination of the complex phase transition under sloshing conditions.

1. Introduction

Maritime transport accounts for over 80% of worldwide goods transportation since it is cost-effective and energy-efficient [1]. More than 90% of heavy-duty vessels in marine transport use heavy fuel oil (HFO), resulting in significant NO_x and SO_x emissions that account for 15% and 13% of total anthropogenic emissions, respectively [2,3]. In this regard, International Maritime Organization (IMO) has toughened environmental restrictions. SO_x emissions must be lowered from 3.5% to 0.5% since 2020; marine engine NO_x emissions must meet Tier III (3.4 g/kWh) in NO_x emission control area (NECA) and Tier II (14.4 g/kWh) globally [4,5]. The tightened environmental regulation forces ship industry to substitute traditional marine fuel to comply with the emission control in fuel requirement [6]. The natural gas (NG), as the cleanest burning fossil fuel and also abundantly available, is becoming a highly attractive alternative fuel for maritime transportation [7]. Compared with HFO, gas fueled engines offers significant reduction of harmful emissions to the atmosphere, which may decrease particulate matters, SO_x and NO_x emissions by near 99%, 100%, and

80% respectively, and reduce 40% greenhouse gas emissions owing to the removal of H₂S, CO₂ and heavy hydrocarbons in the feed gas purification process [8–10].

The majority of vessels utilize natural gas via liquefied natural gas (LNG) or hybrid diesel-LNG engines, as LNG only takes 1/600 volume of its vapor form under the atmospheric pressure [11,12]. Lean burn spark ignited engines and four-stroke dual fuel engines [13,14] are the first to be used on LNG fueled ships, which require an inlet pressure approximately 6.0 bar. In principle, cryogenic liquids can be self-pressurized due to the nature of low saturation temperature. To maintain the tank pressure, the LNG tank equips a pressure build-up unit (PBU) instead of mechanical pumps [15]. When tank pressure drops below a predetermined threshold during navigation, PBU begins pressurizing the tank by evaporating a portion of LNG into vapor and venting it back to the tank top [16].

While utilizing LNG as a clean fuel, storing and handling such a cryogenic liquid presents operational challenges that largely affects the

* Corresponding author.

E-mail address: godyyc@sjtu.edu.cn (Y. Yuan).

fuel system's reliability. One of the challenges arises from the thermodynamic response of LNG subjected to the sloshing of the fuel tank [17]. The pressurized fuel tank is a thermally non-equilibrium system that contains subcooled LNG and superheated vapor gas, with the vapor's superheat being caused by either heat leakage or PBU operation. At static conditions, the liquid–vapor interface approaches equilibrium by forming a temperature stratification layer beneath and above the liquid surface, accompanied with mild pressure variations. When a tank experiences sloshing, liquid motion disrupts equilibrium and causes direct contact condensation of superheated vapor, which results in sudden pressure drops and may even cause unexpected shutdown of the gas engine [18].

During the last decade, the thermodynamic characteristics of cryogenic fluid storage have drawn attentions of many researchers, covering a number of investigations focusing on cryogenic evaporation [19–22], thermal stratification [23–25] and pressure variations [26–28]. Generally, the pressure variations, temperature stratification and phase transition simultaneous occur in LNG fueled tanks with coupled effects on each other. To understand the mechanisms and predict the thermodynamic performance, researchers conducted cryogenic experiments and measured the temperature and pressure transients inside the tank during storage [29–32]. Several types of mathematical models, with different degrees of assumptions and constraints, were established to quantitatively describe the thermal physical process. One typical type of model, referred to as the thermal equilibrium model [33–35], assumes vapor–liquid equilibrium (VLE) and regards the liquid and vapor phases as a whole. With the VLE simplification, the thermal equilibrium model has a high computation efficiency, which is suitable for long-term prediction of LNG evaporation rate and weathering effect. Another type of model, referred to as the thermal non-equilibrium model [36–38], removes the constraint of VLE and handles the liquid (LNG) and the boil-off gas (BOG) separately, and is hence capable to characterize more dynamics inside the tank such as vapor superheating [24], thermal stratification [38] and pressure variations [25]. By incorporating with the composition conservation equations and the boundary layer equations, the composition variations [39] and natural convection effects [21] that possess significant impact on the boil-off characteristics could be quantitatively described.

Under marine conditions, the sloshing of the cryogenic liquid inside the tank leads to a more complex interaction between the liquid and vapor phases. Most of the studies on tank sloshing focus on the wave breaking characteristics and sloshing-induced pressure loads on tank walls [40–42]. With respect to the sloshing effects on the thermodynamic performance in the cryogenic storage tank, Ludwig et al. [17] experimentally investigated the thermal stratification and pressure transients in a LN_2 tank subjected to periodic excitations. An effective thermal diffusivity was proposed to reflect the sloshing impact on the thermal boundary layer beneath the free surface, and a correlation to calculate the sloshing Nusselt number was proposed. Grotle and Aesøy [43] conducted a laboratory-scale experiment to measure the depressurization and thermal response to sloshing, using water and water vapor as the substituted working fluid, and the results revealed that sloshing can significantly shorten the depressurization period. A zone parameter model was proposed to describe the depressurization process, with the assumption that the thermodynamic parameters are homogeneous in both the liquid and gas zones. As the scale, working conditions and fluid properties deviated somewhat from the practical scenarios, the authors suggested CFD simulations in future works to systematically investigate the sloshing effects in real cases. Wang et al. [44] investigated the periodical pressure evolutions during ship navigation. The zone parameter model was adopted and improved to predict the long-term performance for the sake of calculation efficiency. The temperature gradient in liquid was introduced in the model, and the vapor region was still regarded as a homogeneous zone. Wu and Ju [45] investigated the boil-off characteristics in LNG fuel tank under sloshing conditions by two-dimensional CFD simulations; while the

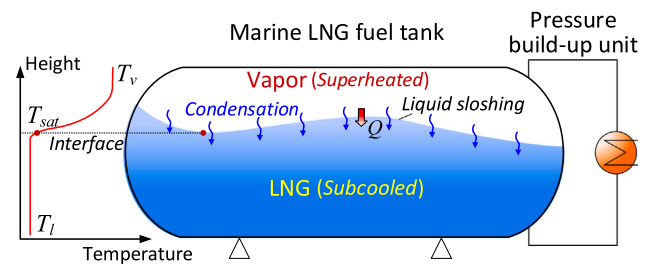


Fig. 1. Schematic diagram of the thermodynamic response in LNG fuel tank under depressurization.

system is characterized by isobaric evaporation, and hence the pressure transients were not included.

The existing researches have shown that sloshing can have a major impact on the thermodynamic performance of LNG fuel tanks, necessitating the development of prediction models and a comprehensive understanding of its influence mechanisms. Based on the literature review, three following aspects have not been involved yet: (1) The existing models, which are based on zone parameter method, have yet to account for the non-uniform temperature fields in liquid and vapor regions, as well as their time evolutions under sloshing. (2) Vapor superheating and its thermal stratification, which had previously been overlooked in experiments and models, may have an unneglectable influence on condensation and depressurization, and is highly dependent on sloshing. (3) Quantitative description of the relations between depressurization, temperature evolution and condensation was detailed in the form of differential equations [43,44], which can be further formulated in algebraic equations to facilitate understanding of their interdependences in a simple way.

Hence, this paper aims to provide a comprehensive investigation of the sloshing effects on the thermodynamic responses in marine LNG fuel tanks, with a particular focus on the three abovementioned aspects. A validated three-dimensional numerical model is proposed in Sections 2 and 3, providing necessary details regarding phase interface morphology and field distribution in real-scale simulations. The major dynamics and their interactions in the sloshing tank, such as liquid motions, phase transition, temperature distribution and depressurization, are numerically analyzed in Section 4. Furthermore, a theoretical equation is derived to characterize the relations between tank depressurization, vapor temperature and condensation in algebraic form, and its effectiveness and applicability are evaluated through numerical data in Section 5.

2. Numerical modeling of tank thermodynamic response under sloshing condition

2.1. Physical problem description

The modeling object is an LNG fuel tank equipped in marine vessels. During navigation, the tank pressure is required to be maintained to ensure the supply of LNG to the engine. Once the tank pressure falls to a certain level, the pressure build-up unit works to vaporize the LNG and inject the vapor back into the tank, thereby increasing the internal pressure. However, the injected vapor and the LNG are in thermal non-equilibrium state, giving rise to the cooling and condensation of the high-temperature vapor, and a subsequent pressure shoot-down in a few minutes. The sloshing of the liquid under sea conditions even accelerates the depressurization process. The thermal physical process is described in Fig. 1.

In the LNG fuel tank, the major dynamics required to be quantitatively described include:

- (1) liquid sloshing and variation of free surface;

- (2) interfacial heat and mass transfer between the liquid and vapor phase;
- (3) vapor temperature and pressure responses due to sloshing and heat-mass transfer.

The 3D numerical approach is capable of predicting the phase interface movement and wave breaking under sloshing conditions, and provides the most detailed information regarding the non-uniform temperature distribution and the condensation rate, allowing for a better understanding of the evolution nature and the dominant effect under different sloshing regimes. Therefore, the 3D numerical model is developed in the present study to quantitatively describe the major dynamics in the LNG fuel tank, as introduced in Section 2.2–Section 2.4.

2.2. Governing equations

In order to investigate the sloshing effects on the thermodynamic response of LNG fuel tank, the volume of fluid (VOF) method which can model the free surface flows of immiscible fluids is employed to track the vapor–liquid interface movement. The continuity equations for each phase are established in the form of volume fraction, as shown in Eqs. (1) and (2).

$$\frac{\partial}{\partial t}(\alpha_v \rho_v) + \nabla \cdot (\alpha_v \rho_v \mathbf{u}_v) = S_m \quad (1)$$

$$\frac{\partial}{\partial t}(\alpha_l \rho_l) + \nabla \cdot (\alpha_l \rho_l \mathbf{u}_l) = -S_m \quad (2)$$

where, ρ is the fluid density, α is the volume fraction of the phase which satisfies $\alpha_v + \alpha_l = 1$, \mathbf{u} is the velocity vector, S_m is the source term of mass transfer between vapor and liquid phases; the subscript v and l represent the vapor phase and liquid phase, respectively.

The momentum equation and the energy equation are shared by two phases and solved throughout the computational domain, as expressed by Eqs. (3) and (4).

$$\frac{\partial(\rho \mathbf{u})}{\partial t} + \nabla \cdot (\rho \mathbf{u} \mathbf{u}) = -\nabla P + \nabla \cdot [\mu (\nabla \mathbf{u} + \nabla \mathbf{u}^T)] + \mathbf{F}_\sigma + \mathbf{F}_{vol} \quad (3)$$

$$\frac{\partial(\rho E)}{\partial t} + \nabla \cdot [\mathbf{u}(\rho E + P)] = \nabla \cdot (\lambda \nabla T) + S_h \quad (4)$$

where, P is pressure, μ is viscosity, \mathbf{F}_{vol} is the body force due to sloshing, E is the internal energy, S_h is the source term related to the latent heat of evaporation or condensation.

To solve the governing equations, the source terms in the continuity, momentum and energy equations are to be determined. The source terms of S_m and S_h are calculated by the phase change model introduced in Section 2.3, and the source term of \mathbf{F}_{vol} is calculated by the sloshing force model introduced in Section 2.4.

2.3. Phase change model

The mass transfer between the liquid and vapor phases is dominantly determined by the evaporation and condensation process. The mass transfer rate is related to the liquid–vapor interface temperature and the saturation temperature corresponding to the pressure. The phase change rate is given as

$$S_m = \begin{cases} \gamma_l \alpha_l \rho_l \frac{T - T_{sat}}{T_{sat}}, & T \geq T_{sat} \text{ for evaporation} \\ \gamma_v \alpha_v \rho_v \frac{T - T_{sat}}{T_{sat}}, & T < T_{sat} \text{ for condensation} \end{cases} \quad (5)$$

where, γ is the mass transfer coefficient representing mass transfer relaxation time (s^{-1}); T_{sat} is the saturation temperature corresponding to the pressure.

The source term of energy equation is determined based on the latent heat absorbed or released during the phase change, yielding Eq. (6).

$$S_h = -S_m h_{fg} \quad (6)$$

For enhancing the stability of the solution, the derivative of the source terms with respect to the dependent variables of the transport equation are also determined and added in the user defined function, as shown in Eq. .

$$\begin{cases} \frac{\partial S_m}{\partial \alpha_l} = \gamma_l \rho_l \frac{T_l - T_{sat}}{T_{sat}}, \quad \frac{\partial S_h}{\partial T} = -\frac{h_{fg} \gamma_l \alpha_l \rho_l}{T_{sat}}, & T \geq T_{sat} \text{ for evaporation} \\ \frac{\partial S_m}{\partial \alpha_v} = \gamma_v \rho_v \frac{T_v - T_{sat}}{T_{sat}}, \quad \frac{\partial S_h}{\partial T} = -\frac{h_{fg} \gamma_v \alpha_v \rho_v}{T_{sat}}, & T < T_{sat} \text{ for condensation} \end{cases} \quad (7)$$

A polynomial correlation is used to account for the varied saturation temperature of liquid in the process, which is fitted by the data of LNG with a typical composition (90% mole fraction of methane) and $R_2 = 0.9999$, as shown in Eq. (8). Besides, a correlation of the latent heat is also defined with $R_2 = 0.9999$, as shown in Eq. (9).

$$T_{sat} = 0.0022P^5 - 0.069P^4 + 0.8426P^3 - 5.2353P^2 + 20.523P + 96.25 \quad (8)$$

$$h_{fg} = 10^{-6}P^4 - 0.0004P^3 + 0.0348P^2 - 2.5144P + 682.2 \quad (9)$$

2.4. Sloshing force model

The movement of the fuel tank with the ship under waves and winds gives rise to the sloshing of the internal liquid. The sloshing effect on the thermodynamic response is included by introducing additional inertia forces resulted from tank movement, as calculated by

$$\mathbf{F}_{vol}(t) = -\rho (\mathbf{g} + \boldsymbol{\varepsilon}(t) \times \mathbf{r} + \boldsymbol{\omega}(t) \times (\boldsymbol{\omega}(t) \times \mathbf{r}) + 2\boldsymbol{\omega}(t) \times \mathbf{u}_r(t)) \quad (10)$$

where, $\boldsymbol{\varepsilon}$ is the angular acceleration, $\boldsymbol{\omega}$ is the angular velocity, \mathbf{u}_r is the velocity in the reference frame of the fuel tank.

Considering that the fuel tank has a large length–radius ratio, the most influential sloshing mode is the swaying in the YOZ plane. The excitation is given in sinusoidal form

$$\theta(t) = \theta_m \sin\left(\frac{2\pi t}{T}\right) \quad (11)$$

$$\boldsymbol{\omega}(t) = \frac{2\pi}{T} \theta_m \cos\left(\frac{2\pi t}{T}\right) \mathbf{i} \quad (12)$$

$$\boldsymbol{\varepsilon}(t) = \frac{4\pi^2}{T^2} \theta_m \sin\left(\frac{2\pi t}{T}\right) \mathbf{i} \quad (13)$$

The position, velocity and gravity in the reference frame of the fuel tank can be decomposed as

$$\mathbf{r} = y\mathbf{j} + z\mathbf{k} \quad (14)$$

$$\mathbf{u}_r = u_y\mathbf{j} + u_z\mathbf{k} \quad (15)$$

$$\mathbf{g} = g \sin \theta(t) \mathbf{j} + g \cos \theta(t) \mathbf{k} \quad (16)$$

The component forces of the additional inertia force can hence be expressed in the cartesian coordinate system, which are compatible with the governing equations, as shown in Eq. (17).

$$\begin{cases} \mathbf{F}_y(t) = -\rho (g \sin \theta(t) + y\omega(t)^2 + z\varepsilon(t) + 2\omega(t)u_y(t)) \mathbf{j} \\ \mathbf{F}_z(t) = -\rho (g \cos \theta(t) + z\omega(t)^2 - y\varepsilon(t) - 2\omega(t)u_z(t)) \mathbf{k} \end{cases} \quad (17)$$

3. Model implementation and verification

3.1. Geometry model

A practical fuel tank equipped on a tug is selected for investigation [44]. The geometry model of the LNG fuel tank is shown in Fig. 2. The fuel tank has a total length of 6.5 m and a radius of 2.6 m. The details of the geometries are listed in Table 1. In the present study, the internal response characteristics are more concerned; considering that the depressurization process lasts a short time, especially for sloshing conditions, the external heat leak-in effect is comparatively slight and hence neglected. The initial state and sloshing condition is listed in Table 1. Seven temperature monitoring points are set uniformly along the tank height at the center axis, and a pressure monitoring point is arranged at the same position of T_1 , as shown in Table 2.

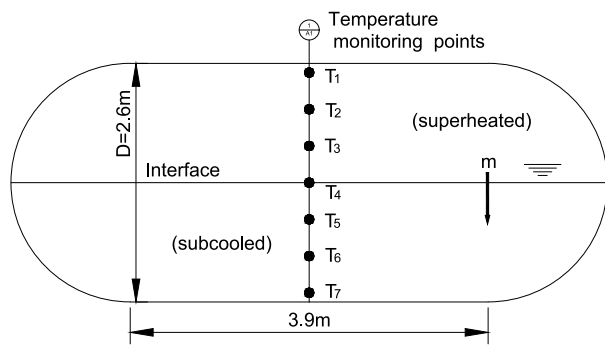


Fig. 2. Geometry diagram of the type-C independent LNG fuel tank on a tug.

Table 1
Tank geometry and conditions for numerical simulation.

	Parameter	Value
Tank geometry	Volume	25 m ³
	Surface area	47 m ²
	Diameter	2.6 m
	Cylindrical section length	3.9 m
Initial conditions	Pressure	8.0 bar
	Vapor temperature	196 K
	Liquid temperature	112 K
Sloshing conditions	Liquid filling level	50%
	Excitation frequency	0.206 Hz
	Excitation amplitude	9°

3.2. Numerical methods

The geometry model and grid generation is implemented in ICEM software. A three-dimensional mesh is adopted to solve the governing equations. The numerical model is solved using the Ansys Fluent double precision solver, but it can also be implemented by other numerical solvers with the capability of dealing with the VOF model. A second-order upwind scheme is selected to discretize the convective terms. The turbulent kinetic energy and the turbulent dissipation rate are also discretized using the second-order upwind scheme. The Pressure-Implicit with Splitting of Operators pressure-velocity PISO scheme is adopted to calculate the pressure field, and the Geo-Reconstruct scheme is suitable for the volume fraction equation. The implicit first order scheme is chosen for transient formulation, with an initial time step of 0.001 s and an upper limit of Courant number set as 0.5. The convergence criteria are judged by monitoring the residuals. When the residuals reduce to less than 10^{-6} for the continuity, momentum and energy equations, it is supposed to meet the convergence criteria.

3.3. Model verification

The numerical model is validated by comparing the numerical results with the experimental data of the sloshing and thermal tests conducted by Grotle and Æsøy [43]. The tank is a laboratory-scale type-C tank with a length of 0.89 m and a diameter of 0.35 m. The sloshing and depressurization process is tested using the water and vapor as the test medium. Detailed working conditions can be found in the literature [43].

Firstly, the liquid sloshing features between the present model predictions and the experimental images are compared, as shown in Fig. 3. The sloshing frequencies are 0.40 Hz and 0.59 Hz respectively, and the sloshing amplitude is 3°. It can be seen that, with the increase of the sloshing frequency f , i.e., the sloshing frequency approaching the first mode natural frequency $f_{1,0}$, the variation of the liquid free surface becomes more violent. The liquid sloshing at 0.40 Hz is featured by an oscillating and continued liquid surface, while liquid jet appears when

the excitation frequency increases to 0.59 Hz. The numerical results show consistency with the captured image of the test, indicating the effectiveness of the sloshing force model used in the present study.

The phase change model is also verified by the depressurization test. Measurement data at the excitation frequency of 0.40 Hz are used, as in this case there is the least amount of residual air in the tank and the resulting effect of non-condensable gas on depressurization is the slightest. The comparison results of the model predictions and the measured data are shown in Fig. 4. The maximum deviation of the predicted pressure with the measured data is about 6.6 kPa, and the maximum deviations of the predicted gas and liquid temperatures with the measured data are 0.73 K and 0.48 K, respectively. The prediction results show that the numerical model is capable to reflect the pressure and phase temperature variations in a close tank.

3.4. Mesh independence analysis

The mesh independence of the physical model is further analyzed. Four different meshes are used and compared adopting the working conditions listed in Table 1. The grid number are 27×10^3 , 113×10^3 , 266×10^3 and 400×10^3 , respectively. The comparison results are shown in Fig. 5.

The results show that when the mesh number increases from 266×10^3 to 400×10^3 , the differences of the calculated pressure are less than 0.4%. Hence, the mesh number of 266×10^3 is selected for numerical investigation on the balance of accuracy and calculation speed. The used structural grid in mesh modeling is illustrated in Fig. 6.

4. Numerical analysis of sloshing effect on tank thermodynamic response

The tank thermodynamic response to sloshing involves phase change, temperature drop and depressurization. The transient features of the interfacial mass transfer and temperature distribution subjected to sloshing are firstly analyzed, and then the resultant tank depressurization are investigated under various conditions.

4.1. Sloshing and interfacial mass transfer

The characteristics of the thermodynamic response to sloshing in the LNG fuel tank are numerically investigated. The sloshing frequency is 0.206 Hz and the sloshing amplitude is 9°. Fig. 7 exhibits the variations of the liquid-vapor interface, interface area and the interfacial mass transfer during several sloshing periods. The variation of the free surface shows that the liquid wave climbs via the spherical side and reaches the roof of the tank, resulting in a reverse jet flow at the top. The jet flow subsequently hits the liquid surface, accompanied by the liquid wave advancing to the other side. The interface area and the condensation rate present cyclical fluctuation along with the sloshing motion. The peak-to-valley amplitudes of the interface area and the condensation rate are little changed, while there is a decreasing trend of the condensation rate along with time. The variation of the condensation rate has a phase lag compared to the surface area variation. The possible reason is that the liquid surface temperature changes due to the contact between the liquid surface and the jet, which delays the decrease of the condensation rate caused by interface area reduction.

4.2. Liquid and vapor temperature evolution

Fig. 8 illustrates the liquid temperature evolution subjected to sloshing. Initially, the liquid beneath the liquid-vapor interface is heated by the vapor, forming a thermally stratified layer. The thermal stratification sustains in the early stage, and the stratified layer shows consistency with the liquid wave. With the time advances, the liquid motion becomes more violent. The liquid jet formed by sloshing adsorbs heat from high-temperature vapor, and falls into the bulk

Table 2
Temperature monitoring points in the LNG fuel tank.

Monitoring points	T_1	T_2	T_3	T_4	T_5	T_6	T_7
Coordinates	(0,0,1.2)	(0,0,0.8)	(0,0,0.4)	(0,0,0)	(0,0,-0.4)	(0,0,-0.8)	(0,0,-1.2)

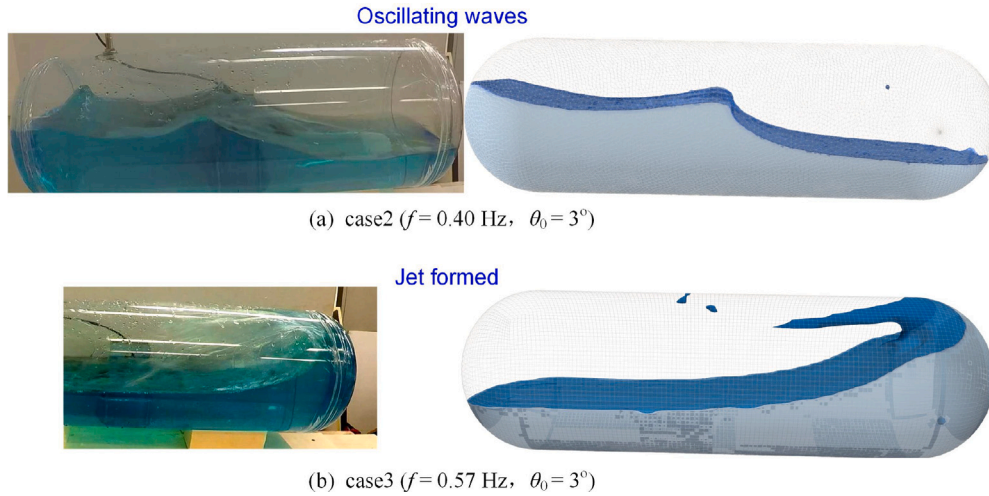


Fig. 3. Comparisons of the liquid sloshing results between numerical and experimental results.

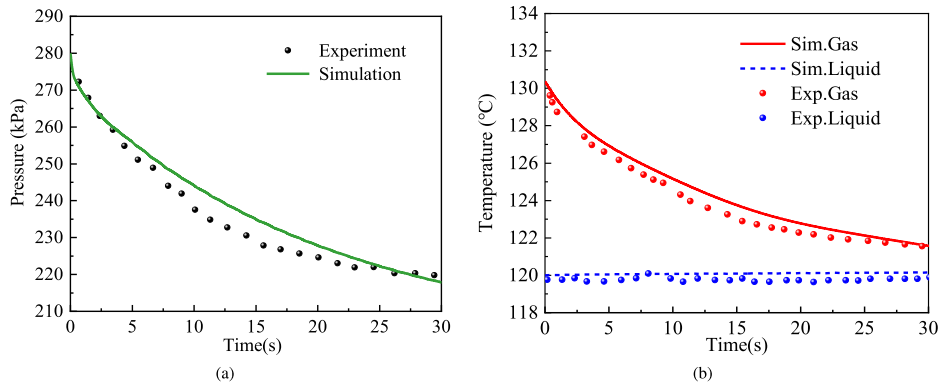


Fig. 4. Comparisons of the transient pressures (a) and temperatures (b) between model predictions and measured data [43].

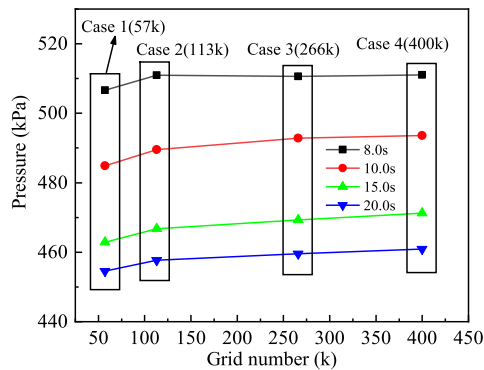


Fig. 5. Numerical results with different mesh number.

liquid, leading to intense mixing of the liquid. The jet flow hence increases the liquid–vapor interface area, and enhances the mass and heat transfer. Consequently, the thermal stratification in liquid diminishes and evolves to uniform temperature distribution. It is also found that, although the temperature of the whole liquid arises, the maximum

temperature located at the interface decreases gradually, reflecting the reduction of temperature non-uniformity.

The results indicate that the liquid temperature evolution subjected to sloshing experiences three stages, namely thermal stratification, sloshing-induced mixing and overall temperature rise; the sloshing strengthens the heat transfer from liquid to vapor, and averages the temperature spatially, resulting in a slight overall temperature rise.

Fig. 9 depicts the vapor temperature evolution subjected to sloshing. The variation of vapor temperature presents two major features: (1) thermal stratification and de-stratification above the free surface; (2) overall temperature drop with time. Similar to the liquid phase, the thermal stratification forms and develops above the liquid surface due to the heat conduction from vapor to liquid. The sloshing not only changes the shape of the free surface, but also alters the temperature distribution in vapor region periodically, enforcing the direction of vapor temperature gradient to be consistent with the normal direction of the free surface. The overall vapor temperature decreases quickly with time due to the enhanced heat transfer by sloshing. De-stratification of the vapor temperature occurs subsequently. Finally, the maximum temperature difference in vapor region is less than 6 °C.

Fig. 10 shows the temperature–time histories for different height positions, where $T_1 - T_3$ are located at the vapor region, T_4 denotes the temperature at the mid-height (the liquid surface), and $T_5 - T_7$

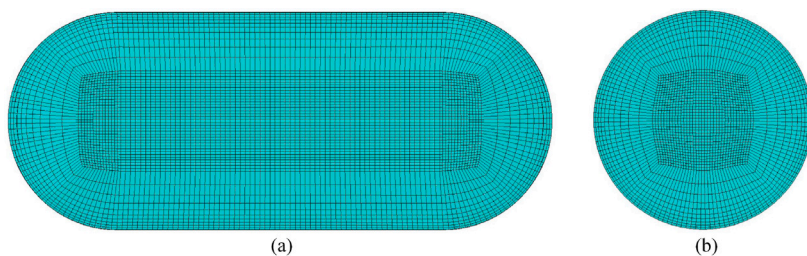


Fig. 6. Mesh model of the LNG fuel tank (266,000 grids): (a) front view (b) side view .

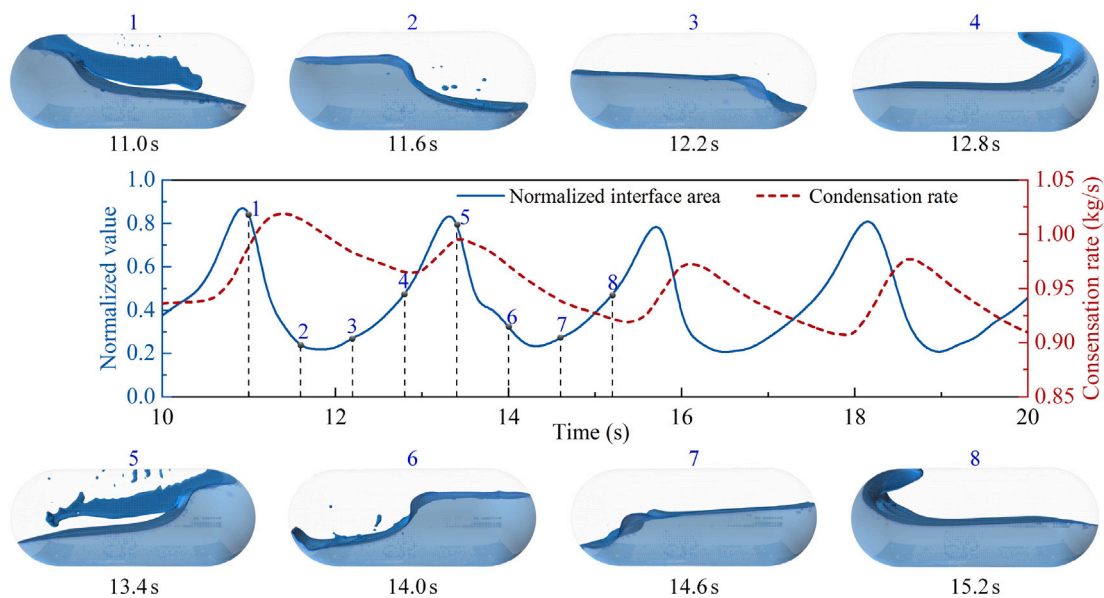


Fig. 7. Variations of free surface and condensation rate subjected to sloshing ($f = 0.206$ Hz, $\theta_m = 9^\circ$).

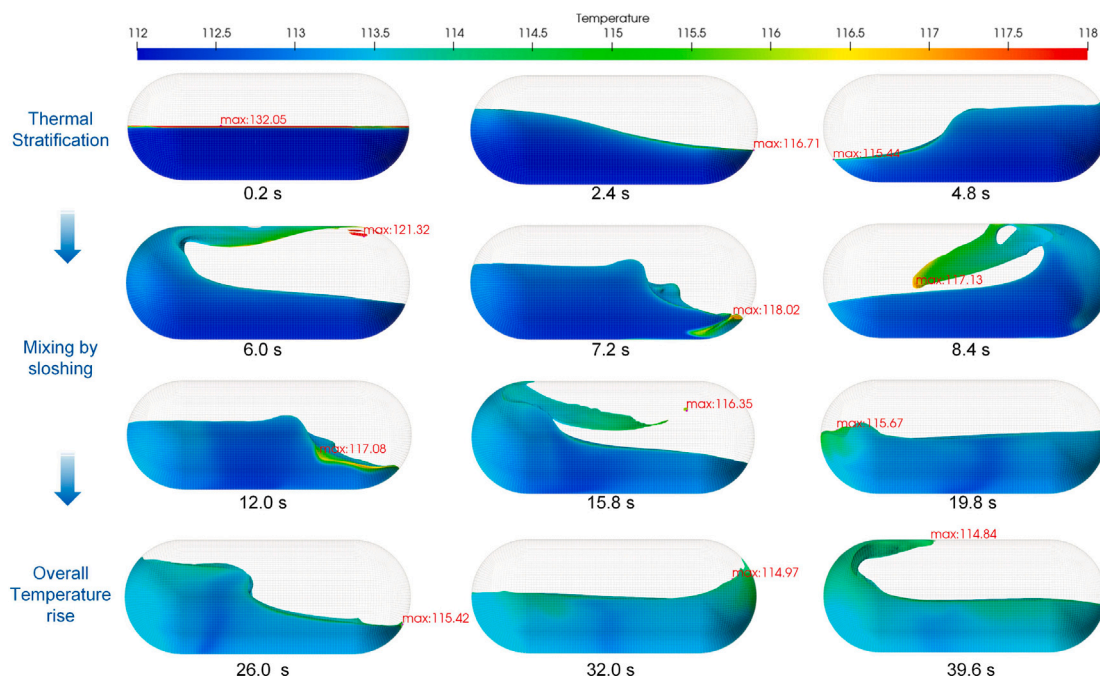


Fig. 8. Liquid temperature evolution subjected to sloshing ($f = 0.206$ Hz, $\theta_m = 9^\circ$).

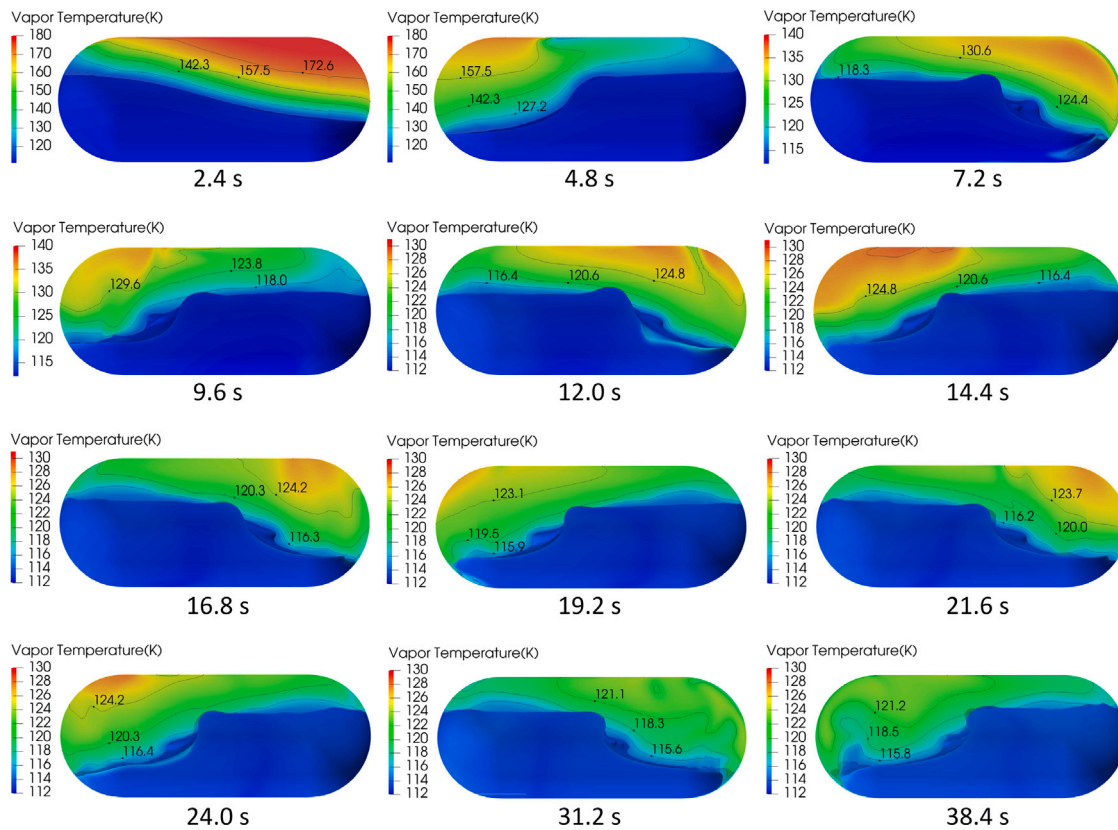


Fig. 9. Vapor temperature evolution subjected to sloshing ($f = 0.206$ Hz, $\theta_m = 9^\circ$).

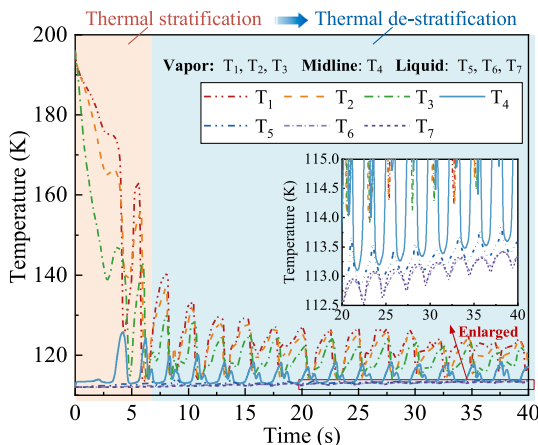


Fig. 10. Variations of temperatures at different heights with time.

are distributed in the liquid. The vapor temperatures fluctuate periodically, of which the variation amplitude increases with the height and decreases with time. The liquid temperatures experience little changes compared to the vapor phase, while has a slight increase with time. The temperature distribution along the height indicates a two-stage evolution feature, i.e., thermal stratification dominated by heat conduction initially, following by the de-stratification of the thermally stratified layer due to sloshing.

4.3. Depressurization by temperature drop and phase transition

The depressurization processes under the static and sloshing conditions are illustrated in Fig. 11(a). Three different mass transfer coefficients are adopted to analyze the effect of condensation rate on

depressurization. The comparisons of the pressure drops between the static and sloshing conditions indicate that sloshing will increase the pressure drop, which is caused by the enhanced interfacial mass and heat transfer. A larger mass transfer coefficient will accelerate the depressurization, and the tank pressure approaches the steady-state value faster. The sloshing effect on depressurization is more significant when the mass transfer coefficient is small. With the increase of mass transfer coefficient, the pressure-time histories under the static and sloshing conditions tend to be closer. The reason can be explained according to the temperature-time-histories shown in Fig. 11(b)–11(d).

When the condensation effect is weak (shown in Fig. 11(b)), the pressure drop is primarily caused by the temperature decrease of the vapor phase. The saturation temperature corresponding to the tank pressure, has a slower falling rate than the vapor temperature, The liquid temperature is almost unchanged due to small heat release from condensation. As a result, the liquid and vapor phases are still in the thermal non-equilibrium state at about 40 s. When the mass transfer coefficient increases to 1.0 (shown in Fig. 11(c)), the condensation is enhanced, and the vapor temperature is close to the saturation temperature. The liquid has a slight temperature rise, but is still in subcooled state that deviates from thermal equilibrium. By enlarging the mass transfer coefficient to 10 (shown in Fig. 11(d)), the condensation caused a rapid pressure drop and the corresponding saturation temperature drop. The latent heat released by condensation heats the liquid and makes the liquid, vapor and saturation temperatures tend to be the same, indicating that the liquid and vapor phases approach the thermal equilibrium state.

To summarize, the sloshing will facilitate the pressure and temperature drop due to the enhanced interfacial mass and heat transfer. The increase of the mass transfer coefficient will weaken the sloshing effect on depressurization, but significantly accelerates the depressurization process until the liquid and vapor phases attain thermal equilibrium. The duration of the thermal non-equilibrium primarily depends on the phase transition rate, which determines the duration of the depressurization process.

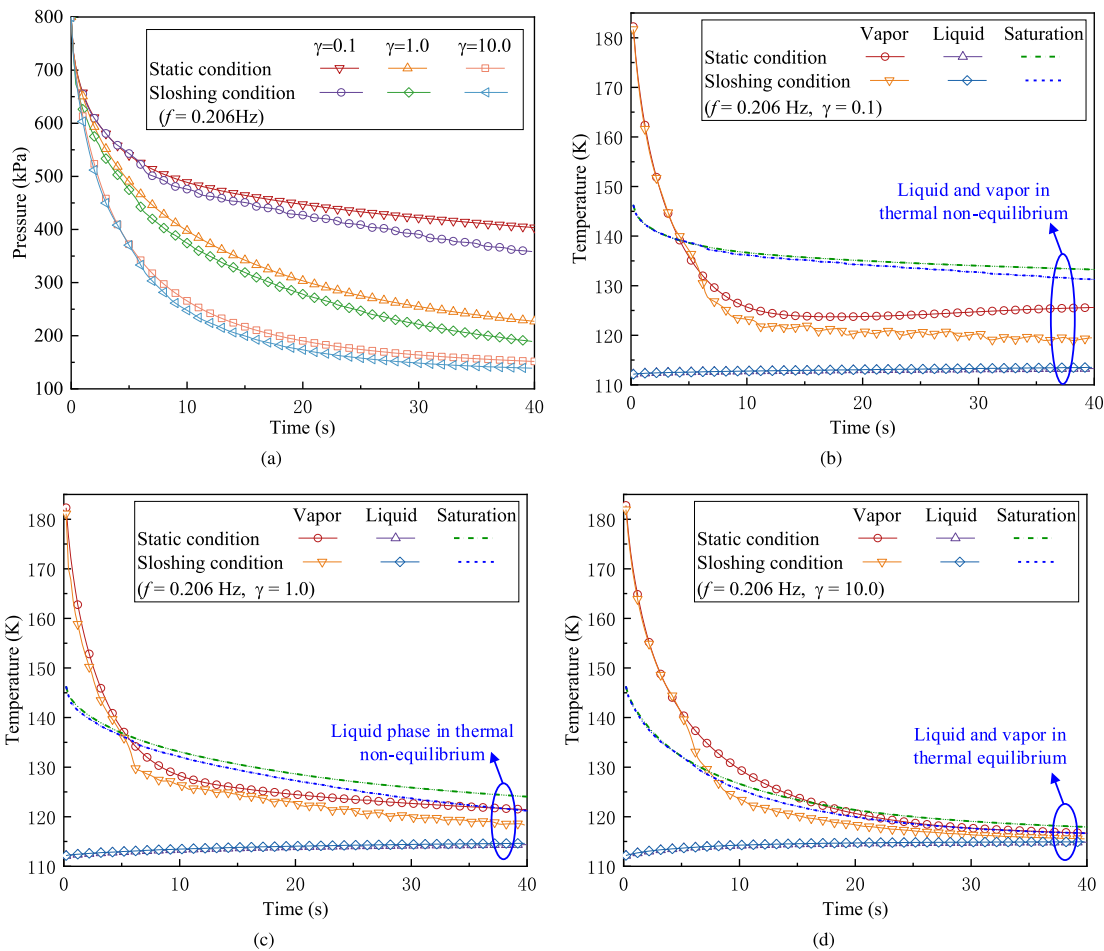


Fig. 11. Pressure and temperature drops under static and sloshing conditions: (a) pressure drops with different mass transfer coefficients (γ); vapor and liquid temperature drop with $\gamma = 0.1$ (b), $\gamma = 1.0$ (c) and $\gamma = 10.0$ (d).

4.4. Effect of sloshing frequency

The fuel tank depressurization under different sloshing frequencies and the static condition are further investigated. The adopted sloshing frequency covers a wide range, which includes the resonance region. The natural frequency is calculated by Eq. (18), where, $a = 1.8\sqrt{1 - h_f/D} + 2.5$, h_f is the liquid depth, D is the diameter of the tank, L_t is the length of the tank.

$$f_n = \frac{1}{T_n} = \frac{1}{a \sqrt{\frac{L_t}{g \tanh\left(\frac{\pi h_f}{L_t}\right)}}} \quad (18)$$

The liquid filling level is set as 50%, and the calculated first mode natural frequency is 0.243 Hz. Referring to Miles [46] weakly non-linear theory, the sloshing mode depends on the dimensionless excitation amplitude and angular wave frequency, as shown in Fig. 12(a). The boundaries of the sloshing modes in Fig. 12(a) are calculated by

$$\left[\omega/\omega_1\right]_i = \left[\left(1.684 \frac{A_f}{R}\right)^{2/3} \beta_i + 1 \right]^{1/2} \quad (19)$$

where, A_f is the maximum tank displacement, R is the radius of the cylindrical tank, $\beta_2 = -0.36$, $\beta_3 = -1.55$ and $\beta_4 = 0.735$ are the bifurcation parameters that depict the boundaries of the sloshing modes.

According to the sloshing mode, three different frequencies, respectively 0.147 Hz, 0.206 Hz and 0.267 Hz are adopted for investigation.

The ratios of the excitation frequency to the first mode natural frequency are 0.6, 0.85 and 1.1, respectively. Fig. 12(b) and (c) illustrate the variations of the phase interface under the three different frequencies. The fluctuation of interface area becomes more violent with the increase of the sloshing frequency. Compared to the sloshing case F2 and F3, the variation of the interface area in case F4 is more irregular, because the sloshing frequency is close to the natural frequency. It is worth noting that the interface area for 0.147 Hz turns to be smaller than the static condition, while the other two sloshing cases have a larger interface area. The reason is that the liquid filling level is 50%, which is the maximum flat surface; the low sloshing frequency only causes the inclination and slight deformation of the liquid surface, leading to a smaller interface area.

Fig. 13 shows the time histories of the pressures, temperatures and condensation rates under different sloshing frequencies. Fig. 13(a) indicates a significant effect of the sloshing frequency on the pressure drop. The increase of the sloshing frequency accelerates the depressurization process and shortens the time to reach steady state. The time for the tank pressure to drop below 180 kPa is 163.4 s, 192.8 s and 240.6 s at sloshing frequencies of 0.267 Hz, 0.206 Hz and 0.146 Hz, respectively. Fig. 13(b) shows the variations of the temperatures of the vapor and liquid phases. The liquid and vapor phase approaches vapor-liquid equilibrium faster at a higher sloshing frequency. The increase of sloshing frequency has a larger impact on the vapor temperature than the liquid. From Fig. 13(c), it can be seen that the vapor temperature has a more violent fluctuation amplitude at a higher sloshing frequency. The valley values of the monitored temperatures at point T_1 at the frequency 0.206 Hz and 0.267 Hz are much lower than those at the

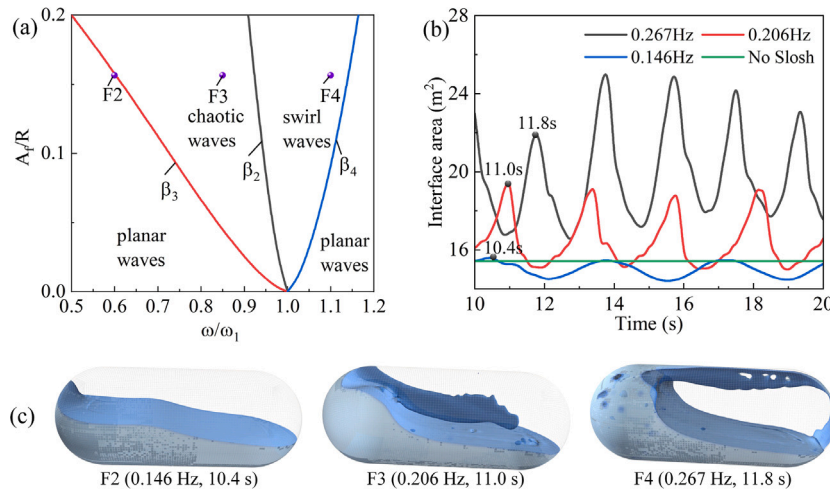


Fig. 12. Liquid-vapor interface characteristics under different sloshing frequencies: (a) sloshing modes, (b) time history of phase interface, (c) phase interface distribution.

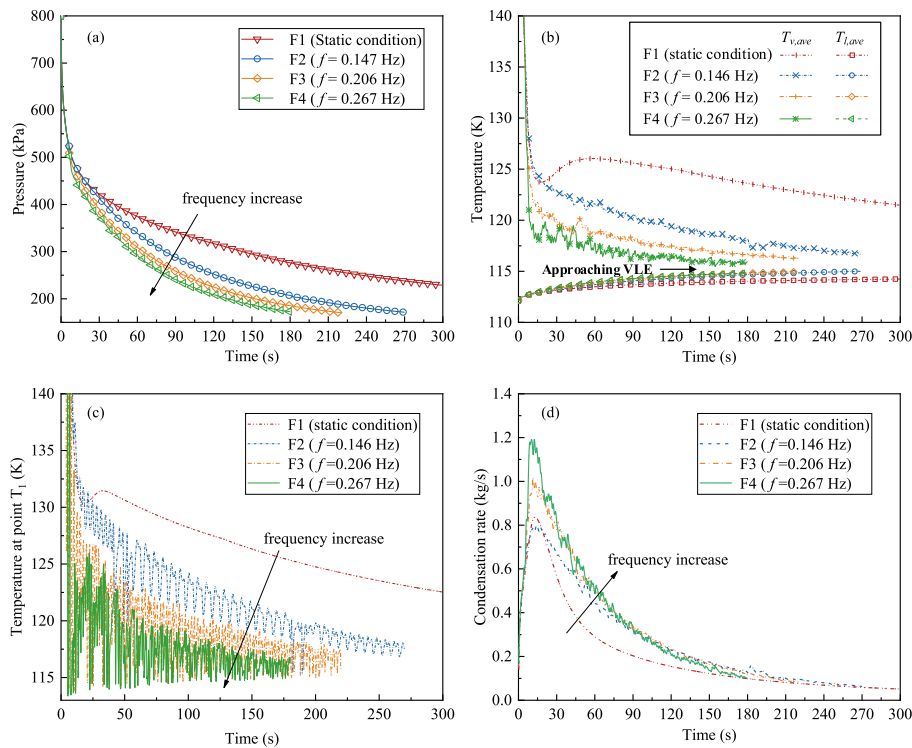


Fig. 13. Thermodynamic responses under different sloshing frequencies: (a) tank pressures; (b) average temperatures of liquid and vapor phases; (c) temperatures at monitoring point T_1 ; (d) condensation rates.

frequency 0.146 Hz, also indicating that the point T_1 is periodically occupied by the cryogenic liquid. At a low sloshing frequency, the temperature fluctuation is regular with a decreasing amplitude. With the sloshing frequency increases, the temperature variation becomes irregular, and the peak values decline faster. The variations of the vapor condensation rate are illustrated in Fig. 13(d). The condensation rate increases rapidly at first and then falls gradually. The increase of sloshing frequency enhances the phase transition rate, especially for high frequencies because liquid jet occurs and largely facilitates the interfacial mass and heat transfer. It is also worth noting that, the condensation rate at a higher sloshing frequency falls faster, because the liquid and vapor phases are closer to the equilibrium state; hence the condensation rates at different sloshing frequencies tends to be the same after about 200 s.

5. Theoretical modeling and analysis of tank depressurization

5.1. Theoretical calculation of tank pressure drop

The theoretical solution of the tank pressure drop is deduced based on mass conservation law. The condensation of vapor gas causes the reduction of vapor mass, as given by Eq. (20).

$$\frac{d(\rho_v V_v)}{dt} = \dot{m}_{cond} \quad (20)$$

As the fuel tank experiences pressure drop in a short time, the phase change leads to little volume change ($\frac{dV_v}{dt} = 0$) and the conservation equation can hence be expressed as

$$\frac{\partial \rho_v}{\partial P} \frac{dP}{dt} + \frac{\partial \rho_v}{\partial T_v} \frac{dT_v}{dt} = -\frac{\dot{m}_{cond}}{V_v} \quad (21)$$

The equation of state (EOS) for vapor gas can be written as

$$P = \frac{\rho_v R_g T_v}{1 - b\rho_v} - f(\rho_v^2) \quad (22)$$

By applying EOS and neglecting the high order term of vapor density, Eq. (20) can be transformed to an expression of the time derivative of tank pressure, as shown in Eq. (23).

$$\frac{dP}{dt} = -\frac{R_g T_v}{(1 - b\rho_v)^2} \frac{\dot{m}_{cond}}{V_v} + \frac{R_g \rho_v}{1 - b\rho_v} \frac{dT_v}{dt} \quad (23)$$

The fuel tank pressure drop can be obtained by integrating Eq. (23) along time

$$\Delta P(t) = \int_0^t \frac{R_g T_v}{(1 - b\rho_v)^2} \frac{\dot{m}_{cond}}{V_v} d\tau + \int_0^t \frac{R_g \rho_v}{1 - b\rho_v} \frac{dT_v}{dt} d\tau \quad (24)$$

As the boil-off gas is at a low pressure and temperature state, the term $b\rho_v \ll 1$; Eq. (24) can hence be rewritten as

$$\Delta P(t) = \frac{R_g}{V_v} \int_0^t T_v \dot{m}_{cond} d\tau + R_g \int_0^t \rho_v \frac{dT_v}{d\tau} d\tau \quad (25)$$

The vapor density is a time-varying parameter depending on the condensation rate, as given by

$$\rho_v(t) = \frac{M_{v,0} - \int_0^t \dot{m}_{cond} d\tau}{V_v} = \rho_{v,0} - \frac{\int_0^t \dot{m}_{cond} d\tau}{V_v} \quad (26)$$

where, the subscript 0 represents the initial state.

Substituting Eq. (26) into Eq. (25), we obtain

$$\Delta P(t) = \frac{R_g}{V_v} \int_0^t T_v \dot{m}_{cond} d\tau + R_g \rho_{v,0} \Delta T_v(t) + \frac{R_g}{V_v} \int_0^t \left(\int_0^t \dot{m}_{cond} d\tau \right) \frac{dT_v}{d\tau} d\tau \quad (27)$$

Introducing the accumulated condensation mass $M_{cond} = \int_0^t \dot{m}_{cond} d\tau$, Eq. (27) becomes

$$\Delta P(t) = \frac{R_g}{V_v} \int_0^t \left(T_v \frac{dM_{cond}}{d\tau} \right) d\tau + R_g \rho_{v,0} \Delta T_v(t) + \frac{R_g}{V_v} \int_0^t \left(M_{cond} \frac{dT_v}{d\tau} \right) d\tau \quad (28)$$

The first and third terms at the right hand side can be merged, yielding the solution of pressure drop

$$\Delta P(t) = \frac{R_g}{V_v} T_v(t) M_{cond}(t) + R_g \rho_{v,0} (T_{v,0} - T_v(t)) \quad (29)$$

According to Eq. (29), predicting the pressure drop requires to determine the vapor volume, the condensation mass and the vapor temperature. It is also worth noting that the initial vapor density instead of the transient vapor density during depressurization can be directly used for calculation. Considering that the vapor volume is almost unchanged in the duration of the depressurization process, the pressure drop is only determined by the condensation mass and the vapor temperature. Fig. 14 illustrates the comparison results of the numerical simulation and the theoretical calculation, where the data of the condensation mass and the vapor temperature are acquired from numerical results. It can be seen that the calculation results of Eq. (29) are consistent with the numerical results, of which the pressure deviations are within ± 20 kPa, i.e., 2.5% of the pressure variation range.

The comparison results indicate that Eq. (29) can be applied for quantitative determination of the phase transition in the thermal non-equilibrium tank subjected to sloshing. By measuring the time histories of the pressure and the vapor temperature inside the fuel tank, the condensation mass and the phase change rate can hence be obtained by Eq. (30).

$$\begin{cases} M_{cond}(t) = \frac{V_v}{R_g T_v(t)} [\Delta P(t) - R_g \rho_{v,0} (T_{v,0} - T_v(t))] \\ \dot{m}_{cond}(t) = \frac{dM_{cond}(t)}{dt} \end{cases} \quad (30)$$

5.2. Approximating prediction of pressure–time histories

In Eq. (29), the transient vapor temperature is required for predicting the pressure drop. Here we further analyze the prediction of the pressure–time histories with an approximating function of the transient vapor temperature.

According to Sections 4.2 and 4.3, the variation of the liquid temperature is quite small comparing to the vapor temperature. The vapor zone presents a prominent temperature stratification, while the liquid temperature is quickly rendered uniform by sloshing. Hence, the vapor temperature nonuniformity should be taking into account, and it is practical to regard the liquid temperature as a constant during the duration of tank depressurization ($T_l \approx T_{l,0}$). In terms of the heat transfer between liquid and vapor phases, heat conduction plays the dominate role. Thus, the vapor temperature could be approximately calculated referring to the solution of semi-infinite heat conduction problem with the first type boundary condition, as given by

$$\frac{T_v(t, z) - T_l}{T_{v,0}(z) - T_l} = \operatorname{erf} \left(\frac{z}{2\sqrt{a_{v,e}t}} \right) \quad (31)$$

where, $a_{v,e}$ represents the effective vapor thermal diffusivity under sloshing, z is the height above the free surface.

Let $T_v(t, z) - T_l = \theta(t, z)$ and $z/a_{v,e}t = i^*(z)$, where $i^*(z)$ is a dimensionless parameter, the integral-average temperature difference between liquid and vapor along height is expressed as

$$\begin{aligned} \hat{\theta}(t) &= \theta_0 \frac{2\sqrt{a_{v,e}t}}{H_v} \int_0^{i^*(H_v)} \operatorname{erf}(i^*) di^* \\ &= \theta_0 \left(\operatorname{erf}(i^*(H_v)) + \frac{e^{-i^{*2}(H_v)} - 1}{i^*(H_v)\sqrt{\pi}} \right) \end{aligned} \quad (32)$$

where, θ_0 represents the initial temperature difference between liquid and vapor; H_v is the height of the vapor region. The terms $T_v(t)$ and $T_{v,0} - T_v(t)$ in Eq. (29) are replaced by

$$T_v(t) = \theta_0 \left(\operatorname{erf}(i^*(H_v)) + \frac{e^{-i^{*2}(H_v)} - 1}{i^*(H_v)\sqrt{\pi}} \right) + T_{l,0} \quad (33)$$

$$T_{v,0} - T_v(t) = \theta_0 \left(\frac{e^{-i^{*2}(H_v)} - 1}{i^*(H_v)\sqrt{\pi}} - \operatorname{erfc}(i^*(H_v)) \right) \quad (34)$$

Substituting Eqs. (33) and (34) into Eq. (29), the pressure–time histories can be obtained by

$$\begin{aligned} \Delta P(t) &= \frac{R_g}{V_v} M_{cond}(t) \left[\theta_0 \left(\operatorname{erf}(i^*(H_v)) + \frac{e^{-i^{*2}(H_v)} - 1}{i^*(H_v)\sqrt{\pi}} \right) + T_{l,0} \right] \\ &\quad - R_g \rho_{v,0} \theta_0 \left(\operatorname{erfc}(i^*(H_v)) - \frac{e^{-i^{*2}(H_v)} - 1}{i^*(H_v)\sqrt{\pi}} \right) \end{aligned} \quad (35)$$

The pressure–time histories predicted by Eq. (35) are compared to the numerical results, as shown in Fig. 15. The predicted pressures deviate from the numerical results within the range of -60 kPa to $+20$ kPa (-7.5% – 2.5% of the pressure variation range) under different sloshing frequencies and mass transfer rate. The increasing deviations compared to Eq. (29) are primarily caused by the approximating function of the transient vapor temperature (see Fig. 15).

The time-average pressure deviations and the corresponding best-fitted effective thermal diffusivity are given in Fig. 16(a). The time-average pressure deviations are within 14 kPa. It can be seen that the effective thermal diffusivity increases with the increases of the sloshing frequency and the decrease of the mass transfer coefficient. The reason is that the sloshing enhances the heat exchange between the liquid and vapor phase, and the condensation releases heat that impedes the heat transfer between the two phases. Fig. 16(b) shows the sensitivity analysis of the effective thermal diffusivity on the time-average pressure deviations. The increase of sloshing frequency makes the prediction results more sensitive to the effective thermal diffusivity.

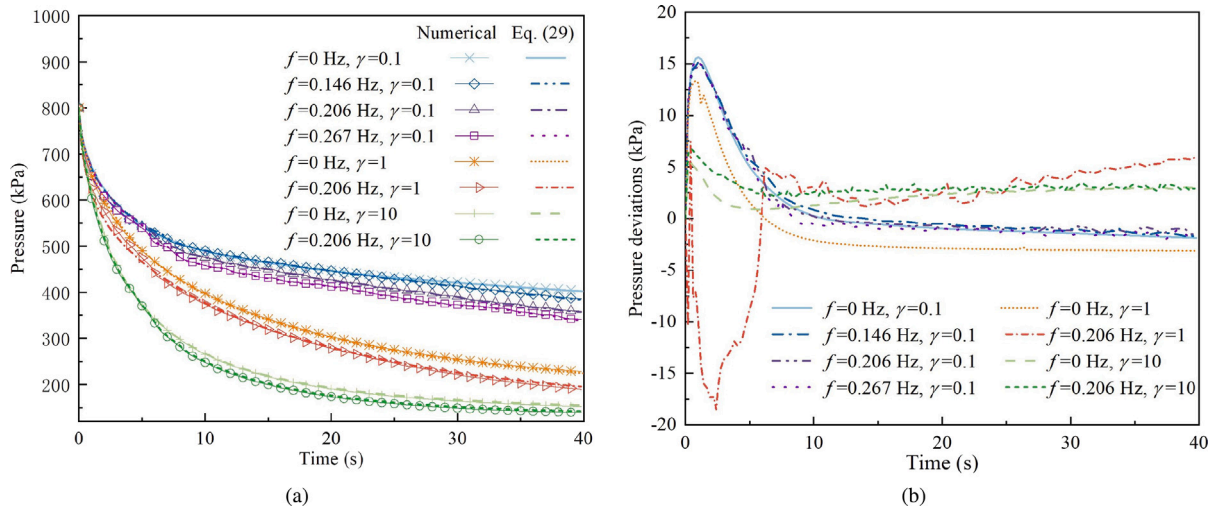


Fig. 14. Comparisons between the numerical simulation and the theoretical calculation: (a) evolution of pressure drops; (b) pressure deviations.

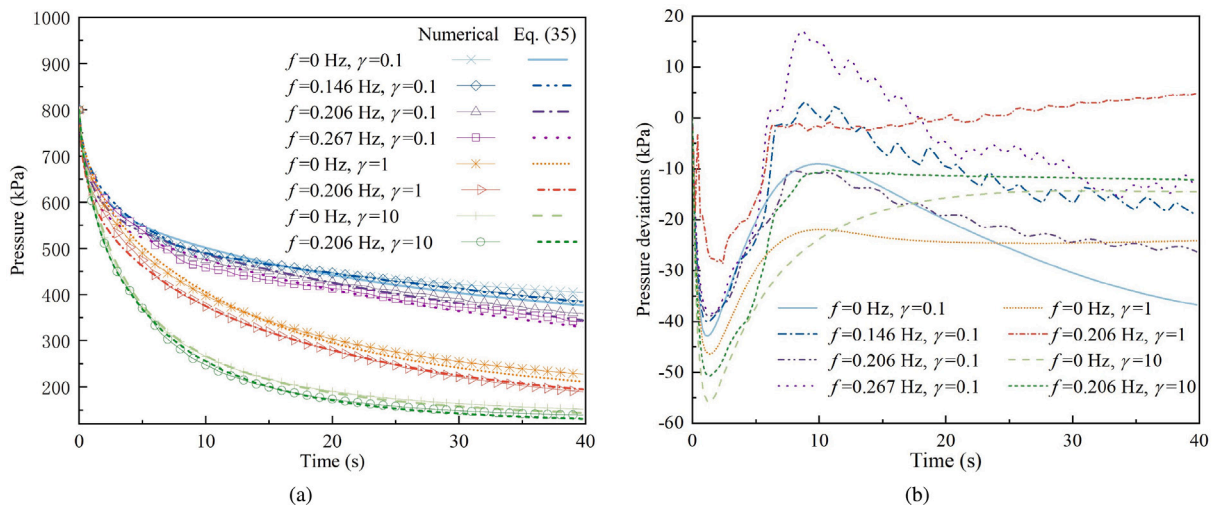


Fig. 15. Comparisons between the numerical simulation and the approximation prediction: (a) evolution of pressure drops; (b) pressure deviations.

Within a range that covers all the best-fitted values of the effective thermal diffusivity, the maximum time-average pressure deviation is less than 40 kPa, which is 5% of the pressure variation range. The results indicate that the calculation of vapor temperature based on the semi-infinite heat conduction simplification is feasible for predicting tank depressurization under sloshing conditions.

6. Conclusion

In this paper, the sloshing effects on the coupled pressure–temperature response in LNG fuel tank were numerically and theoretically investigated. A numerical model using the CFD technique was presented accounting for the liquid sloshing movement and the interfacial mass and heat transfer. The validity of the model was confirmed by the corresponding experimental data. Three-dimensional simulations of the depressurization process in a practical LNG fuel tank under sloshing conditions were performed. The coupled dynamics of pressure variation, temperature evolution and phase transition were analyzed. A theoretical expression that quantitatively describes the relations of the pressure, temperature and condensation were proposed. Following are the salient conclusions drawn from the analyses:

(1) Liquid temperature undergoes three stages during the depressurization process, namely thermal stratification, sloshing-induced

mixing and overall temperature rise. The sloshing strengthens the heat transfer from liquid to vapor, and averages the temperature spatially, resulting in a slight overall temperature rise.

- (2) Vapor temperature forms a stratified layer that alters periodically with the variation of the free surface shape. The overall temperature declines rapidly accompanied with the decrease of the temperature gradient in the vapor region. Finally the vapor temperature presents cyclical fluctuations along with the sloshing motion.
- (3) Tank depressurization is caused by the mutual effects of temperature drop and phase transition. The depressurization continues until the liquid and vapor phase achieves thermal equilibrium. At the early stage, the temperature drop is the dominant effect, and then the vapor condensation effect becomes prominent. A larger condensation rate brings forward the time to achieve thermal equilibrium, while weakens the sloshing effect on depressurization.
- (4) Sloshing frequency has a significant effect on the pressure–temperature response, especially when the excitation frequency is close to resonance conditions. A higher sloshing frequency accelerates the depressurization process and shortens the time to reach thermal equilibrium. The increase of sloshing frequency also alters the liquid sloshing mode, which produces liquid jet

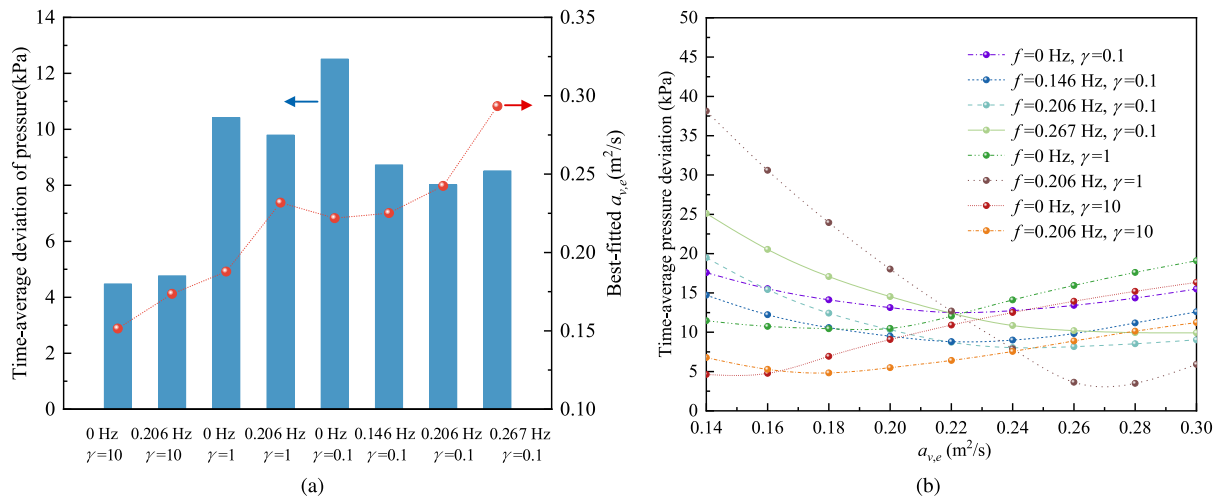


Fig. 16. Time-average pressure deviations and the corresponding best-fitted effective thermal diffusivity ($a_{v,e}$) (a); sensitivity analysis of $a_{v,e}$ on the pressure deviations (b).

flow and makes the vapor temperature variation more violently and irregularly. The phase transition is enhanced by sloshing at the early stage, and then tends to be slight and little affected by sloshing frequency.

- (5) The theoretical equation of the pressure drop quantitatively describes relations between pressure drop, temperature variation and phase transition. The relative deviations of the calculated pressure with the numerical results are less than 2.5% of the pressure variation range under various sloshing frequencies and mass transfer coefficients. The coupled pressure–temperature response can be further predicted by introducing an equivalent thermal diffusivity that reflects the sloshing effect on vapor temperature evolution. The calculation results indicate that the deviations of the pressure drop are among -7.5% – 2.5% of the pressure variation range.

The proposed theoretical equation characterizes the quantitative relations between pressure drop, temperature drop and condensation, but it is noted that its application for predicting tank depressurization still requires accurate correlations or data of the phase transition rate. According to the theoretical equation, the pressure drop at arbitrary time only depends on the transient vapor temperature and the condensation mass. With known initial parameters including the vapor volume and the initial vapor density, the condensation mass and the transient condensation rate can be inversely determined by measuring the vapor temperature and the tank pressure. Considering that the phase transition between the thermal non-equilibrium liquid and vapor phases is complex and strongly coupled with the liquid sloshing, the theoretical equation can offer a feasible approach of quantifying the phase transition rate under sloshing conditions by inversion method, and may give a guidance for future works to develop condensation correlations in LNG fuel tanks under a wide range of sloshing and working conditions.

Nomenclature

$a_{v,e}$	Effective thermal diffusivity (m ² /s)
A_f	Maximum tank displacement (m)
b	Repulsion parameter (m ³ /kg)
D	Tank diameter (m)
E	Internal energy (J/kg)

f	Frequency (Hz)
F_σ	Term of surface tension (N/m ³)
F_{vol}	Term of body force (N/m ³)
g	Gravitational acceleration (m/s ²)
h_f	Liquid depth (m)
h_{fg}	Latent heat (J/kg)
H_v	Height of the vapor region (m)
i, j, k	Unit vector
L_t	Tank length (m)
\dot{m}	Condensation rate (kg/s)
M	Mass (kg)
P	Pressure (kPa)
\mathbf{r}	Position
R	Radius (m)
R_g	Gas constant (J/(kg K))
S_m	Mass source term (kg/(m ³ s))
S_h	Energy source term (J/(m ³ s))
t	Time (s)
t^*	Dimensionless time
T	Temperature (K)
\mathbf{u}	Velocity (m/s)
V	Volume (m ³)
z	The height above the free surface (m)
Greek symbols	
α	Volume fraction
β	Bifurcation parameter
γ	Mass transfer coefficient (s ⁻¹)
ϵ	Angular acceleration (rad/s ²)
μ	Viscosity (Pa s)
λ	Thermal conductivity (W/(m K))
ρ	Density (kg/m ³)
θ	Angle (rad)
θ_0	Initial temperature difference between liquid and vapor (K)
$\hat{\theta}$	Integral-average temperature difference (K)
ω	Angular velocity (rad/s)
τ	Time (s)

Abbreviations

BOG	Boil-off gas
HFO	Heavy fuel oil
LNG	Liquefied natural gas
PBU	Pressure build-up unit
VLE	Vapor liquid equilibrium
VOF	Volume of fluid

Subscripts

0	Initial state
cond	Condensation
m	Maximum
l	Liquid
sat	Saturation
v	Vapor
y,z	Coordinates

CRedit authorship contribution statement

Zhongdi Duan: Conceptualization, Methodology, Project administration, Funding acquisition, Writing – original draft. **Yifeng Zhu:** Resources, Investigation, Writing – review & editing. **Chenbiao Wang:** Investigation, Validation, Data curation, Software. **Yuchao Yuan:** Funding acquisition, Resources, Conceptualization, Writing – review & editing. **Hongxiang Xue:** Funding acquisition, Writing – review & editing. **Wenyong Tang:** Supervision, Writing – review & editing.

Declaration of competing interest

The authors declare that they have no known competing financial interests or personal relationships that could have appeared to influence the work reported in this paper.

Data availability

Data will be made available on request.

Acknowledgments

The authors gratefully acknowledge the supports from the National Natural Science Foundation of China (Grant No. 52001207), Young Elite Scientists Sponsorship Program by CAST and CSSC-SJTU Marine Equipment Prospective Innovation Joint Fund (1-B1).

References

- Mondejar M, Andreasen J, Pierobon L, Larsen U, Thern M, Haglid F. A review of the use of organic Rankine cycle power systems for maritime applications. *Renew Sustain Energy Rev* 2018;91:126–51. <http://dx.doi.org/10.1016/j.rser.2018.03.074>, URL <https://linkinghub.elsevier.com/retrieve/pii/S136403211830162X>.
- Yoo BY. Economic assessment of liquefied natural gas (LNG) as a marine fuel for CO₂ carriers compared to marine gas oil (MGO). *Energy* 2017;121:772–80. <http://dx.doi.org/10.1016/j.energy.2017.01.061>, URL <https://linkinghub.elsevier.com/retrieve/pii/S0360544217300610>.
- Thomson H, Corbett JJ, Winebrake JJ. Natural gas as a marine fuel. *Energy Policy* 2015;87:153–67. <http://dx.doi.org/10.1016/j.enpol.2015.08.027>, URL <https://linkinghub.elsevier.com/retrieve/pii/S0301421515300665>.
- Hiraoka N, Miyanagi A, Kuroda K, Ito K, Nakagawa T, Ueda T. The World's First Onboard Verification Test of UE Engine with Low Pressure EGR complied with IMO's NO_x Tier III Regulations. 53, (2):2016, p. 8.
- Senda T, Harumi K. Prospects and Challenges for the Future of Marine Power Systems. *J Japan Inst Mar Eng* 2018;53(3):279–84. <http://dx.doi.org/10.5988/jime.53.279>, URL https://www.jstake.jst.go.jp/article/jime/53/3/53_279/article.
- Seo S, Chu B, Noh Y, Jang W, Lee S, Seo Y, Chang D. An economic evaluation of operating expenditures for LNG fuel gas supply systems onboard ocean-going ships considering availability. *Ships Offshore Struct* 2016;11(2):213–23. <http://dx.doi.org/10.1080/17445302.2014.984389>, URL <http://www.tandfonline.com/doi/full/10.1080/17445302.2014.984389>.
- Burel F, Taccani R, Zuliani N. Improving sustainability of maritime transport through utilization of Liquefied Natural Gas (LNG) for propulsion. *Energy* 2013;57:412–20. <http://dx.doi.org/10.1016/j.energy.2013.05.002>, URL <https://linkinghub.elsevier.com/retrieve/pii/S0360544213003861>.
- Æsøy V, Stenersen D. Low Emission LNG Fuelled Ships for Environmental Friendly Operations in Arctic Areas. In: Volume 6: Polar and arctic sciences and technology; offshore geotechnics; petroleum technology symposium. Nantes, France: American Society of Mechanical Engineers; 2013. <http://dx.doi.org/10.1115/OMAE2013-11644>, V006T07A028 URL <https://asmedigitalcollection.asme.org/OMAE/proceedings/OMAE2013/55409/Nantes,%20France/279433>.
- Khor J, Dal Magro F, Gundersen T, Sze J, Romagnoli A. Recovery of cold energy from liquefied natural gas regasification: Applications beyond power cycles. *Energy Convers Manage* 2018;174:336–55. <http://dx.doi.org/10.1016/j.enconman.2018.08.028>, URL <https://linkinghub.elsevier.com/retrieve/pii/S019689041830877X>.
- Atienza-Márquez A, Bruno JC, Coronas A. Cold recovery from LNG-regasification for polygeneration applications. *Appl Therm Eng* 2018;132:463–78. <http://dx.doi.org/10.1016/j.applthermaleng.2017.12.073>, URL <https://linkinghub.elsevier.com/retrieve/pii/S1359431117366140>.
- Duan Z, Ding G, Tang W, Ren T. A thermodynamic model for predicting transient pressure evolution in response to venting and vaporization of liquefied gas under sudden release. *J Hard Mater* 2020;395:122460. <http://dx.doi.org/10.1016/j.jhazmat.2020.122460>.
- Wang X, Xu Y, Wang S, Xu Q, Ho TC. Comprehensive study on boil-off gas generation from LNG road tankers under simultaneous impacts of heat leakage and transportation vibration. *Fuel* 2020;275:117876, 10/gkc96b URL <https://linkinghub.elsevier.com/retrieve/pii/S0016236120308723>.
- Mitsubishi. Mitsubishi KU series line-up [EB/OL]. 2019, URL http://www.mhiet.co.jp/en/products/engine/generation/plant/pdf/ku_lineup_en.
- Rolls-Royce. Diesel and gas engines [EB/OL]. 2017, URL <https://www.rolls-royce.com/~media/Files/R/Rolls-Royce/documents/marine-product-finder/diesel-and-gas-engines-brochure-1216.pdf>.
- Ehlers S, Asbjørnslett BE, Rodseth OJ, Berg TE, editors. Modelling of LNG fuel systems for simulations of transient operations. In: *Maritime-Port Technology and Development*. 0. CRC Press; 2014, p. 213–24. <http://dx.doi.org/10.1201/b17517-26>, URL <https://www.taylorfrancis.com/books/9781315731629/chapters/10.1201/b17517-26>.
- Grotle EL, Æsøy V, Halse KH, Pedersen E, Li Y. Non-isothermal sloshing in marine liquefied natural gas fuel tanks. In: *Proceedings of the twenty-sixth (2016) international ocean and polar engineering conference*. Rhodes, Greece: the International Society of Offshore and Polar Engineers (ISOPE); 2016.
- Ludwig C, Dreyer M, Hopfinger E. Pressure variations in a cryogenic liquid storage tank subjected to periodic excitations. *Int J Heat Mass Transfer* 2013;66:223–34. <http://dx.doi.org/10.1016/j.ijheatmasstransfer.2013.06.072>, URL <https://linkinghub.elsevier.com/retrieve/pii/S0017931013005498>.
- DiRenzo J, Neksà P, Kolsaker K. Analysis of Natural Gas Engine De-Loading on LNG Fuelled Vessels. *Energy Procedia* 2015;64:73–82. <http://dx.doi.org/10.1016/j.egypro.2015.01.010>, URL <https://linkinghub.elsevier.com/retrieve/pii/S1876610215000119>.
- Lin Y, Ye C, Yu Y-y, Bi S-w. An approach to estimating the boil-off rate of LNG in type C independent tank for floating storage and regasification unit under different filling ratio. *Appl Therm Eng* 2018;135:463–71. <http://dx.doi.org/10.1016/j.applthermaleng.2018.02.066>, URL <https://linkinghub.elsevier.com/retrieve/pii/S1359431117371818>.
- Huerta F, Vesovic V. Analytical solutions for the isobaric evaporation of pure cryogenics in storage tanks. *Int J Heat Mass Transfer* 2019;143:118536. <http://dx.doi.org/10.1016/j.ijheatmasstransfer.2019.118536>, URL <https://linkinghub.elsevier.com/retrieve/pii/S0017931019333812>.
- Duan Z, Xue H, Gong X, Tang W. A thermal non-equilibrium model for predicting LNG boil-off in storage tanks incorporating the natural convection effect. *Energy* 2021;233:121162. <http://dx.doi.org/10.1016/j.energy.2021.121162>, URL <https://linkinghub.elsevier.com/retrieve/pii/S0360544221014109>.
- Saleem A, Farooq S, Karimi IA, Banerjee R. A CFD simulation study of boiling mechanism and BOG generation in a full-scale LNG storage tank. *Comput Chem Eng* 2018;115:112–20. <http://dx.doi.org/10.1016/j.compchemeng.2018.04.003>, URL <https://linkinghub.elsevier.com/retrieve/pii/S0098135418302564>.
- Choi SW, Lee WI, Kim HS. Numerical analysis of convective flow and thermal stratification in a cryogenic storage tank. *Numer Heat Transfer Part A Appl* 2017;71(4):402–22. <http://dx.doi.org/10.1080/10407782.2016.1264771>, URL <https://www.tandfonline.com/doi/full/10.1080/10407782.2016.1264771>.
- Huerta F, Vesovic V. A realistic vapour phase heat transfer model for the weathering of LNG stored in large tanks. *Energy* 2019;174:280–91. <http://dx.doi.org/10.1016/j.energy.2019.02.174>, URL <https://linkinghub.elsevier.com/retrieve/pii/S0360544219303809>.
- Duan Z, Sun H, Cheng C, Tang W, Xue H. A moving-boundary based dynamic model for predicting the transient free convection and thermal stratification in liquefied gas storage tank. *Int J Therm Sci* 2021;160:106690. <http://dx.doi.org/10.1016/j.ijthermalsci.2020.106690>, URL <https://linkinghub.elsevier.com/retrieve/pii/S129007292031139X>.
- Joseph J, Agrawal GS, Agarwal D, Pisharady JC, Kumar SS. Effect of insulation thickness on pressure evolution and thermal stratification in a cryogenic tank. *Appl Therm Eng* 2017;111:1629–39.
- Deng P, Liang J, Wu Y, Li T. Dynamic boil-off characterization for discharge process of LNG vehicle tank. *Energy* 2019;186:115813.
- Jo YP, Bangi MSF, Son SH, Kwon JSI, Hwang SW. Dynamic modeling and offset-free predictive control of LNG tank. *Fuel* 2021;285:119074, 10/gmx5tw URL <https://linkinghub.elsevier.com/retrieve/pii/S0016236120320706>.
- Das SP, Chakraborty S, Dutta P. Studies on Thermal Stratification Phenomenon in LH₂ Storage Vessel. *Heat Transf Eng* 2004;25(4):54–66. <http://dx.doi.org/10.1080/01457630490443767>, URL <http://www.tandfonline.com/doi/abs/10.1080/01457630490443767>.

- [30] Kang M, Kim J, You H, Chang D. Experimental investigation of thermal stratification in cryogenic tanks. *Exp Therm Fluid Sci* 2018;96:371–82. <http://dx.doi.org/10.1016/j.expthermflusci.2017.12.017>, URL <https://linkinghub.elsevier.com/retrieve/pii/S0894177717304004>.
- [31] Konopka M, Noeding P, Klätte J, Behruzi P, Gerstmann J, Stark A, Darkow N. Analysis of LN2 Filling, Draining, Stratification and Sloshing Experiments. In: 46th AIAA Fluid dynamics conference. Washington, D.C.: American Institute of Aeronautics and Astronautics; 2016. <http://dx.doi.org/10.2514/6.2016-4272>, URL <https://arc.aiaa.org/doi/10.2514/6.2016-4272>.
- [32] Seo M, Jeong S. Analysis of self-pressurization phenomenon of cryogenic fluid storage tank with thermal diffusion model. *Cryogenics* 2010;50(9):549–55. <http://dx.doi.org/10.1016/j.cryogenics.2010.02.021>, URL <https://linkinghub.elsevier.com/retrieve/pii/S0011227510000603>.
- [33] Dimopoulos G, Frangopoulos CA. A dynamic model for liquefied natural gas evaporation during marine transportation. *Int J Thermodyn* 2008;11:123–31.
- [34] Adom E, Islam SZ, Ji X. Modelling of Boil-Off Gas in LNG Tanks: A Case Study. *Int J Eng Technol* 2010;2(4):292–6.
- [35] Migliore C, Tubilleja C, Vesovic V. Weathering prediction model for stored liquefied natural gas (LNG). *J Nat Gas Sci Eng* 2015;26:570–80. <http://dx.doi.org/10.1016/j.jngse.2015.06.056>.
- [36] Migliore C, Salehi A, Vesovic V. A non-equilibrium approach to modelling the weathering of stored Liquefied Natural Gas (LNG). *Energy* 2017;124:684–92. <http://dx.doi.org/10.1016/j.energy.2017.02.068>, URL <https://linkinghub.elsevier.com/retrieve/pii/S0360544217302426>.
- [37] Effendy S, Khan MS, Farooq S, Karimi IA. Dynamic modelling and optimization of an LNG storage tank in a regasification terminal with semi-analytical solutions for N2-free LNG. *Comput Chem Eng* 2017;99:40–50. <http://dx.doi.org/10.1016/j.compchemeng.2017.01.012>, URL <https://linkinghub.elsevier.com/retrieve/pii/S0098135417300121>.
- [38] Wang Z, Sharafian A, Mérida W. Thermal stratification and rollover phenomena in liquefied natural gas tanks. *Energy* 2022;238:121994.
- [39] Miana M, del Hoyo R, Rodríguez V. Comparison of evaporation rate and heat flow models for prediction of Liquefied Natural Gas (LNG) ageing during ship transportation. *Fuel* 2016;177:87–106. <http://dx.doi.org/10.1016/j.fuel.2016.02.070>, URL <https://linkinghub.elsevier.com/retrieve/pii/S0016236116001988>.
- [40] Royon-Lebeaud A, Hopfinger EJ, Cartellier AH. Liquid sloshing and wave breaking in circular and square-base cylindrical containers. *J Fluid Mech* 2007;577:467–94.
- [41] Wang C, Yu Guo C, Han FL. LNG tank sloshing simulation of multidegree motions based on modified 3D MPS method. *Math Probl Eng* 2020;2020:1–14.
- [42] Ibrahim RA. Assessment of breaking waves and liquid sloshing impact. *Nonlinear Dynam* 2020;100:1837–925.
- [43] Grotle EL, Aesøy V. Dynamic modelling of the thermal response enhanced by sloshing in marine LNG fuel tanks. *Appl Therm Eng* 2018;135:512–20. <http://dx.doi.org/10.1016/j.applthermaleng.2018.02.086>, URL <https://linkinghub.elsevier.com/retrieve/pii/S1359431117330065>.
- [44] Wang C, Ju Y, Fu Y. Dynamic modeling and analysis of LNG fuel tank pressurization under marine conditions. *Energy* 2021;232:121029, 10/gkx39t URL <https://linkinghub.elsevier.com/retrieve/pii/S0360544221012779>.
- [45] Wu S, Ju Y. Numerical study of the boil-off gas (BOG) generation characteristics in a type C independent liquefied natural gas (LNG) tank under sloshing excitation. *Energy* 2021;223:120001.
- [46] Miles J. Resonantly forced surface waves in a circular cylinder. *J Fluid Mech* 1984;149:15–31.